



# CHORUS

This is the accepted manuscript made available via CHORUS. The article has been published as:

## Impact of $^{68}\text{Se}$ and $^{72}\text{Kr}$ stellar weak interaction rates on rp-process nucleosynthesis and energetics

A. Petrovici, A. S. Mare, O. Andrei, and B. S. Meyer

Phys. Rev. C **100**, 015810 — Published 31 July 2019

DOI: [10.1103/PhysRevC.100.015810](https://doi.org/10.1103/PhysRevC.100.015810)

# Impact of $^{68}\text{Se}$ and $^{72}\text{Kr}$ stellar weak interaction rates on rp-process nucleosynthesis and energetics

A. Petrovici<sup>1,2</sup>, A.S. Mare<sup>1,2</sup>, O. Andrei<sup>1</sup>, and B.S. Meyer<sup>3</sup>

<sup>1</sup>*Horia Hulubei National Institute for Physics and Nuclear Engineering, R-077125 Bucharest, Romania*

<sup>2</sup>*Faculty of Physics, University of Bucharest, R-077125 Bucharest, Romania*

<sup>3</sup>*Department of Physics and Astronomy, Clemson University, Clemson, SC 29634-0978, USA*

(Dated: July 16, 2019)

The impact of beyond-mean-field predictions of stellar weak interaction rates of  $^{68}\text{Se}$  and  $^{72}\text{Kr}$  waiting point nuclei on the rp-process in type-I x-ray bursts is investigated including the contribution of thermally populated low-lying states for both  $\beta^+$  decay and continuum electron capture. The realistic description of the effects of shape coexistence and mixing in the structure of parent and daughter nuclei on the stellar weak rates is obtained within the *complex* Excited Vampir model. We performed a series of post-processing calculations revealing significant effects on the energy generation, reaction flow, and final composition of the burst ashes.

## I. INTRODUCTION

In recent years the investigation of proton-rich  $N \approx Z$  nuclei in the  $A \approx 70$  mass region has received an increasing interest both theoretically and experimentally not only due to their exotic structure and dynamics but also due to the particular role played during the rapid proton capture process (rp-process) in type-I x-ray bursts (XRBs) and their associated nucleosynthesis [1–5]. These explosive phenomena take place on the surface of neutron stars accreting hydrogen/helium-rich material from a low-mass close companion star. Nucleosynthesis in explosive hydrogen burning at high temperatures and densities is characterized mainly by the rp-process, a sequence of proton captures and weak interaction processes including  $\beta^+$  decays and continuum electron captures (cEC). The present study focuses on weak interaction rates of proton-rich nuclei, particularly waiting points like  $^{68}\text{Se}$  and  $^{72}\text{Kr}$ , which play a critical role in rp-process nucleosynthesis. The competition between the proton capture rates and the rates of the weak interaction processes at the waiting points determines rp-process reaction flows, and, consequently, the characteristic physical observables of the XRBs. In particular, it influences the nuclear energy production rate that ultimately translates into the luminosity profile with time, the main direct observable of a type I x-ray burst. The luminosity profile in turn can constrain the properties of the underlying neutron star. This competition also determines the burst time scale, the extent of the abundance flow to heavier masses as well as the final composition of the burst ashes needed to model neutron star crust properties [1, 2].

Previous investigations of rp-process nucleosynthesis [3] have used simple estimates of weak interaction rates [6, 7], shell-model calculations for nuclei in the  $A = 45$ – $65$  mass range [8] and laboratory ground state rates for  $A \approx 70$   $N = Z$  nuclei. Reliable predictions of the characteristics of nuclei beyond experimental reach require self-consistent nuclear structure models that are able to describe the properties of experimentally accessible proton-rich nuclei. Robust predictions on Gamow-Teller

strength distributions for the ground state and the thermally populated low-lying excited states in the stellar environment, temperature dependance of the  $\beta^+$ -decay rates as well as temperature and density evolution of the continuum electron capture rates during the rp-process are needed to realistically evaluate the impact of weak interaction rates of the waiting point nuclei on nucleosynthesis in XRBs. The comprehensive description of the structure and dynamics of the  $^{68}\text{Se}$  and  $^{72}\text{Kr}$  nuclei requires beyond-mean-field models able to treat realistically the shape coexistence phenomena dominating their behaviour. Weak interaction rates for these nuclei have been calculated based on the QRPA approach using spherical/deformed mean fields for parent and daughter nuclei [9–12]. In recent years we have extensively explored and successfully described various coexistence phenomena revealed by the structure and dynamics of proton-rich nuclei in the  $A \approx 70$  mass region within the *complex* Excited Vampir model (EXVAM) and many of our predictions have been experimentally confirmed [13–20].

In the present paper we explore for the first time the influence of  $^{68}\text{Se}$  and  $^{72}\text{Kr}$  stellar weak interaction rates obtained in the frame of the *complex* Excited Vampir model on the rp-process nucleosynthesis and energetics. The theoretical framework will be presented in the next section. In Sec. III we shall discuss significant effects on characteristic physical observables of x-ray bursts. Some concluding remarks are presented in Sec. IV.

## II. THEORETICAL FRAMEWORK

Essential for the Gamow-Teller strength distributions is a realistic description of the evolution in structure with increasing spin and excitation energy in the parent and daughter nuclei manifesting shape coexistence and mixing, as it is already established for  $^{68}\text{Se}$  and  $^{72}\text{Kr}$  as well as their daughters  $^{68}\text{As}$  and  $^{72}\text{Br}$ , respectively ([17] and references therein). This goal can be reached using beyond-mean-field approaches, realistic effective interactions, and large enough model spaces. These studies have

been accomplished in the frame of the *complex* Excited Vampir variational model using the effective interaction constructed from a nuclear matter G-matrix based on the Bonn A/Bonn CD potential in a model space above the  $^{40}\text{Ca}$  core built out of the  $1p_{1/2}$ ,  $1p_{3/2}$ ,  $0f_{5/2}$ ,  $0f_{7/2}$ ,  $1d_{5/2}$  and  $0g_{9/2}$  oscillator orbits for the valence protons and neutrons [16–19].

To explore the impact of the  $^{68}\text{Se}$  and  $^{72}\text{Kr}$  stellar weak interaction rates on burst simulations we used a post-processing approach based on a one-zone model that was adjusted to match a 1-D multizone hydrodynamic result discussed in [21] as closely as possible [2]. The calculations employ temperature and density profile, relating the history of the neutron star’s accreted envelope with the time evolution of the temperature and the density in a single layer of the envelope, very similar to Schatz *et al.* [2]. Such calculations have been used extensively to overcome the time limitations introduced by computationally intensive hydrodynamic calculations and have been applied to estimate the impact of nuclear uncertainties on the final x-ray burst yields [4, 22]. Our nuclear reaction network includes proton rich nuclei from hydrogen to xenon based on the reaction rates from the JINA Reaclib Database [23]. We used the ignition conditions from Schatz *et al.* [2], density of  $1.1 \times 10^6 \text{ g/cm}^3$  and peak temperature of 1.9 GK, with a rise time scale of  $\approx 4$  s, and a cooling phase lasting  $\approx 200$  s. They assumed an accretion rate of 10% of the Eddington mass ( $m_{\text{Edd}} = 8.8 \times 10^4 \text{ g/cm}^2$ ), initial hydrogen mass fraction  $X = 0.66$ , helium mass fraction  $Y = 0.339$ , and a metallicity  $Z = 0.001$ . Under these conditions there is a natural termination of the rp-process due to a SnSbTe cycle. Since the amount of hydrogen at ignition can vary, which strongly affects the extent of the rp-process [5], we studied the influence of  $^{68}\text{Se}$  and  $^{72}\text{Kr}$  weak interaction rates on energy production, reaction flow and final abundances using the temperature and density profile from [2] varying the initial hydrogen/helium mixing and the metallicity. Four different combinations of H/He mixing and metallicity were examined: hhez1, employs the conditions of Schatz *et al.* [2], mentioned above; hhez2 has also  $Z = 0.001$  ( $^{14}\text{N}$ ) and very similar H/He mixing,  $X = 0.64$  and  $Y = 0.359$ ; hhez3 with solar metallicity,  $Z = 0.02$  ( $^{14}\text{N}$ ),  $X = 0.7048$ , and  $Y = 0.2752$  as well as hhez4 with low metallicity,  $Z = 0.001$  ( $^{14}\text{N}$ ),  $X = 0.759$ , and  $Y = 0.24$  correspond to the compositions used by Woosley *et al.* [3]. For each case we ran a one-zone post-processing calculation using codes and tools developed by B. S. Meyer *et al.* [24] and compared the results obtained using EXVAM weak interaction rates with the ones based on standard rates (laboratory ground state rates).

### III. RESULTS AND DISCUSSION

In the present investigations we introduced the temperature dependance of the weak interaction rates consider-

ing the ground state and the yrast  $2^+$  state of  $^{68}\text{Se}$  (using the Bonn CD potential) while for  $^{72}\text{Kr}$  the ground state, the first excited  $0^+$  and yrast  $2^+$  state (using the Bonn A potential) have been included using their experimental excitation energies [17]. Within the *complex* Excited Vampir model we obtained good agreement with the experimental results on spectra and electromagnetic properties of the positive parity states as well as the terrestrial half-lives and the measured Gamow-Teller strength distributions for these waiting point nuclei describing realistically the oblate-prolate coexistence and mixing dominating their structure and dynamics ([17] and references therein). In chains of independent variational calculations we constructed the wave functions for  $1^+$ ,  $2^+$ , and  $3^+$  daughter states in  $^{68}\text{As}$  and  $^{72}\text{Br}$ , respectively. The results indicate oblate-prolate coexistence and variable, in some cases strong mixing in the structure of both, parent and daughter states. The calculated excitation energy of the yrast  $2^+$  state in  $^{68}\text{Se}$  is 1.021 MeV, while the experimental value is 0.854 MeV. The calculated  $B(E2; 2_1^+ \rightarrow 0_{gs}^+)$  value of  $503 e^2 \text{ fm}^4$  (effective extra charge of  $0.3 e$  is used) compares well with the experimental value of  $432 (58) e^2 \text{ fm}^4$  [25]. In  $^{72}\text{Kr}$  the first excited  $0^+$  state is obtained at an excitation energy of 0.971 MeV, whereas experimentally it occurs at 0.671 MeV, and the yrast  $2^+$  state at 0.604 MeV, while the experimental value is 0.710 MeV. The EXVAM  $B(E2; 2_1^+ \rightarrow 0_{gs}^+)$  value of  $670 e^2 \text{ fm}^4$  is in good agreement with the new experimental result of  $810 (150) e^2 \text{ fm}^4$  [26]. Using the latest experimental results on mass measurements [27–30] the EXVAM terrestrial half-life of  $^{68}\text{Se}$  amounts to 34.9 s while the experimental value is  $35.5(7)$  s [31] and for  $^{72}\text{Kr}$  we obtained 18.6 s compared to the measured value of  $17.1(2)$  s [32]. Quenching was not applied since our investigations on the Gamow-Teller decay of  $^{72}\text{Kr}$  revealed very small changes for the strength distributions in an extended model space including the spin-orbit partners [17]. A missing Gamow-Teller strength of  $\approx 10\%$  attributed to the  $\Delta$  excitation [33] is not included in the present results. The experimental results on the Gamow-Teller strength distribution for  $^{68}\text{Se}$  are established only up to 0.426 MeV excitation energy [34] from the whole  $\beta$  window of  $Q_{\text{EC}} = 4.705 (2)$  MeV. For  $^{72}\text{Kr}$  the high resolution data [35] cover 3.3 MeV and the total absorption spectrometer results 2.7 MeV [36] excitation energy from the total  $Q_{\text{EC}} = 5.121 (8)$  MeV, but the observed feeding is normalized to 100% in both cases. Significant differences appear between the results obtained with the two methods for some energy regions. The EXVAM results manifest a reasonable agreement with the experimental data given the errors and the assumptions in the analysis of the data [17]. New measurements covering the full  $\beta$  window could give support to our results based on a realistic description of the shape coexistence and mixing dominating the structure of parent and daughter states. Figure 1 shows the EXVAM decay rates decomposed into the corresponding  $\beta^+$  and cEC components for selected densities as a function of temperature. The

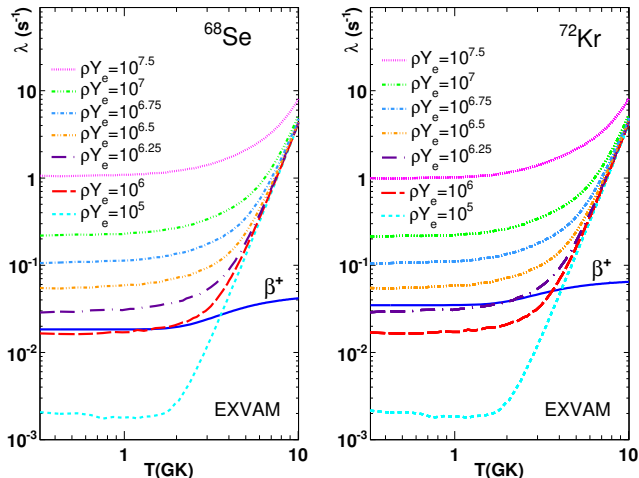


FIG. 1. The *complex* Excited Vampir decay rates ( $s^{-1}$ ) for the ground state and yrast  $2^+$  state of  $^{68}\text{Se}$  (left) and the ground state, first excited  $0^+$  state, and yrast  $2^+$  state of  $^{72}\text{Kr}$  (right) decomposed into the corresponding  $\beta^+$  and cEC components for selected densities  $\rho Y_e$  ( $\text{mol}/\text{cm}^3$ ) as a function of temperature  $T$  (GK).

two-dimensional representation of the evolution of the EXVAM continuum electron capture rates as a function of temperature and density for  $^{68}\text{Se}$  used in the calculations for the rp-process scenarios is presented in Fig. 2. A similar behaviour is manifested by the cEC rates for  $^{72}\text{Kr}$ . The EXVAM results indicate that the considered low-lying states could make a contribution to the total weak rates of maximum 1.5% for  $^{68}\text{Se}$  and 5.2% for  $^{72}\text{Kr}$  in the relevant temperature and density range.

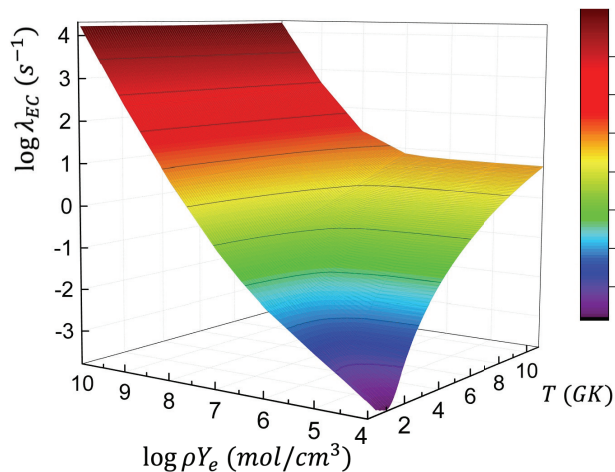


FIG. 2. The evolution of *complex* Excited Vampir cEC rates of  $^{68}\text{Se}$  as a function of temperature  $T$  (GK) and density  $\rho Y_e$  ( $\text{mol}/\text{cm}^3$ ).

Figure 3 presents the  $^{68}\text{Se}$  weak decay flow based on EXVAM weak interaction rates for  $^{68}\text{Se}$  versus standard

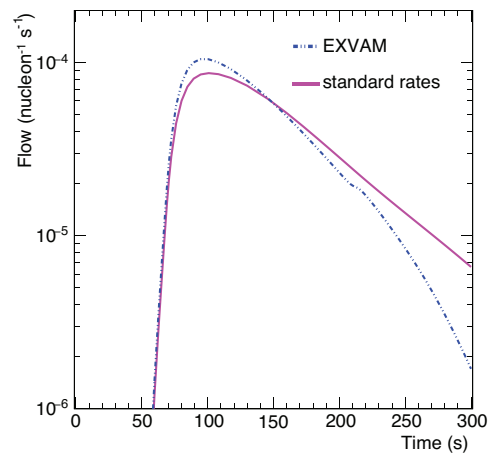


FIG. 3.  $^{68}\text{Se}$  weak decay flow (computed as the total  $^{68}\text{Se}$  weak decay rate times the abundance of  $^{68}\text{Se}$  per nucleon) as a function of time during an x-ray burst obtained using the  $^{68}\text{Se}$  EXVAM weak interaction rates (dotted-dashed line) compared to that based on standard rates (full line) for hhez1 conditions.

rates case in hhez1 conditions as a function of time. The EXVAM flow exceeds the standard flow from 40-90 s after the burst begins at  $\approx 35$  s. The higher flow pushes more matter to higher mass. Of course later, the faster EXVAM rate causes the abundance, and thus the flow of  $^{68}\text{Se}$  to fall faster. Similar results have been obtained for the other initial compositions.

Figure 4 illustrates the hydrogen and helium abundances as a function of time during the x-ray burst for hhez1 and hhez3 mixing conditions. The EXVAM results influence significantly the hydrogen consumption for low metallicity and the lowest considered initial abundances of H, corresponding to hhez1 and hhez2 conditions. Enhanced weak decay flow through  $^{68}\text{Se}$  and  $^{72}\text{Kr}$  with the EXVAM rates leads to faster consumption of free protons after  $\approx 40$  s.

Since the energy generation and the reaction network are coupled self-consistently, we analysed the sensitivity of energy generation rates to the predicted EXVAM weak interaction rates. Figure 5 presents the energy generation rate curves corresponding to the hhez2 and hhez3 combinations of H/He and metallicity. Maximum deviation produced by EXVAM results with respect to the standard ones is obtained for solar composition (20% in the middle point of the burst duration), Fig. 5 (right), while maximum change in shape is obtained for low metallicity and H/He mixing close to the one used by Schatz et al. [2], as it is illustrated in Fig. 5 (left). Enhanced reaction flow through  $^{68}\text{Se}$  and  $^{72}\text{Kr}$  with the EXVAM rates leads to more energy production as the flow reaches the  $A \approx 70$  region than in the case with standard rates. Because of the larger flow to higher mass with the EXVAM rates, protons are consumed faster than with the standard rates (see Fig. 4), which then causes the energy generation

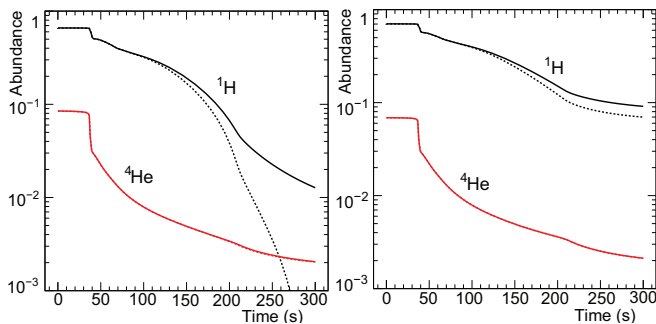


FIG. 4. The abundances of hydrogen and helium as a function of time during an x-ray burst obtained using the  $^{68}\text{Se}$  and  $^{72}\text{Kr}$  EXVAM weak interaction rates (dotted line) compared to that based on standard rates (full line) (left - hhez1, right - hhez3 composition).

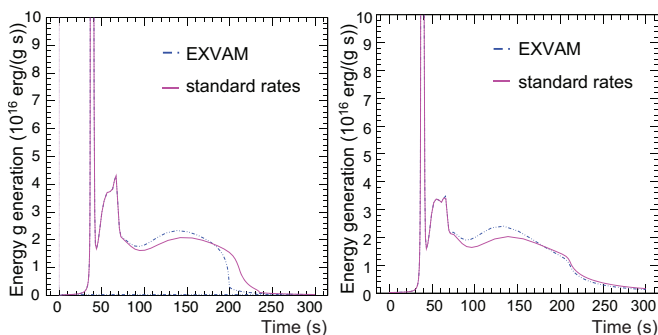


FIG. 5. Energy generation rate curve as a function of time during an x-ray burst obtained using the  $^{68}\text{Se}$  and  $^{72}\text{Kr}$  EXVAM weak interaction rates (dotted-dashed line) compared to that based on standard rates (full line) (left - hhez2, right - hhez3 composition).

to decline earlier than in the case with the standard rates.

Figure 6 shows the integrated reaction currents during an x-ray burst for the hhez1 composition [2]. The thickness of an arrow scales linearly with the magnitude of the integrated current. The  $^{68}\text{Se}$  integrated weak decay current with EXVAM exceeds the standard one by  $5.5 \times 10^{-4}$  nuclei per nucleon. EXVAM weak interaction rates of  $^{68}\text{Se}$  and  $^{72}\text{Kr}$  significantly increase the abundance flow through these two waiting point nuclei in all investigated scenarios. We calculated the total integrated production and destruction reaction currents during an x-ray burst ( $\approx 210$  sec from the ignition) for all considered compositions. Maximum variation in the final abundances was obtained for  $^{68}\text{Se}$  and  $^{72}\text{Kr}$ . In the hhez1 scenario [2] the ratio between the results based on standard weak rates and the ones including EXVAM rates is 3.8 for  $^{68}\text{Se}$  and 3.3 for  $^{72}\text{Kr}$ . Similar results have been obtained for  $^{68}\text{Se}$  and  $^{72}\text{Kr}$  in the other scenarios. The abundance flow presented in Fig. 7 indicates smaller variations for other illustrated waiting points. Results close to Schatz et al. [2] have been obtained

for  $^{103}\text{Sn}$ ,  $^{104}\text{Sn}$ , and  $^{105}\text{Sn}$  isotopes. Similar effects produced using solar abundances (hhez3 scenario) are illustrated in Fig. 8 (right), but in this case, as for hhez4 conditions ( $Z=0.001$  and the highest  $X=0.759$ ) there is still hydrogen to be burned. The abundance flow corresponding to hhez2 (Fig. 8, left) and hhez4 compositions for waiting point nuclei indicate also significant effects on  $^{68}\text{Se}$  and  $^{72}\text{Kr}$ . Once  $^{68}\text{Se}$  has built up by rp-process flows, the enhanced flow through that waiting point isotope with the EXVAM rates causes it to decline faster than with standard rates. This causes higher mass waiting point nuclei to be built up earlier. The effects on the daughter nuclei of the  $^{68}\text{Se}$  and  $^{72}\text{Kr}$  waiting points have been evaluated calculating the integrated current in the  $^{68}\text{As} + ^1\text{H} \rightarrow ^{69}\text{Se} + \gamma$  and  $^{72}\text{Br} + ^1\text{H} \rightarrow ^{73}\text{Kr} + \gamma$  reactions. In the hhez1, hhez3, and hhez4 scenarios, where is still hydrogen to be burned,  $(5.4 - 5.9) \times 10^{-4}$  more  $^{68}\text{As}$  nuclei per nucleon go up to higher mass with EXVAM weak rates than with the standard ones. Similarly for  $^{72}\text{Br}$  we found  $(6.2 - 7.7) \times 10^{-4}$  more current going up to higher mass using EXVAM weak rates for  $^{68}\text{Se}$  and  $^{72}\text{Kr}$  than without.

Since the post-processing calculations only track fixed thermodynamic histories, they do not allow for feedback of the energy generation on the time dependence of the temperature and density during the calculations. As a consequence, the results obtained introducing our theoretical predictions on weak interaction rates that significantly affect the energy production, burst duration, and final abundances should be interpreted with that caveat in mind. Nevertheless, our results are helpful in identifying nuclear properties that govern the XRB energetics.

#### IV. CONCLUSIONS

This work presents the first results on the effects of stellar weak interaction rates for  $^{68}\text{Se}$  and  $^{72}\text{Kr}$  waiting point nuclei self-consistently predicted within the beyond-mean-field *complex* Excited Vampir model taking into account the temperature dependance of the  $\beta^+$  rates as well as temperature and density dependance of continuum electron capture rates on the rp-process in type I x-ray bursts. The contribution of the involved thermally populated low-lying states in  $^{68}\text{Se}$  and  $^{72}\text{Kr}$  is evaluated based on a realistic description of the oblate-prolate coexistence and mixing in the structure of the parents and daughter nuclei. A post-processing approach based on the model of Schatz et al. [2] and four different accreted compositions of H/He and metallicity were employed. A comparison of the results obtained using the *complex* Excited Vampir predictions to the ones based on standard values for the  $\beta^+$ -decay rates is outlined discussing the energy generation rates, the hydrogen and helium consumption, and the abundance flow for waiting point nuclei as well as Sn isotopes reached during the

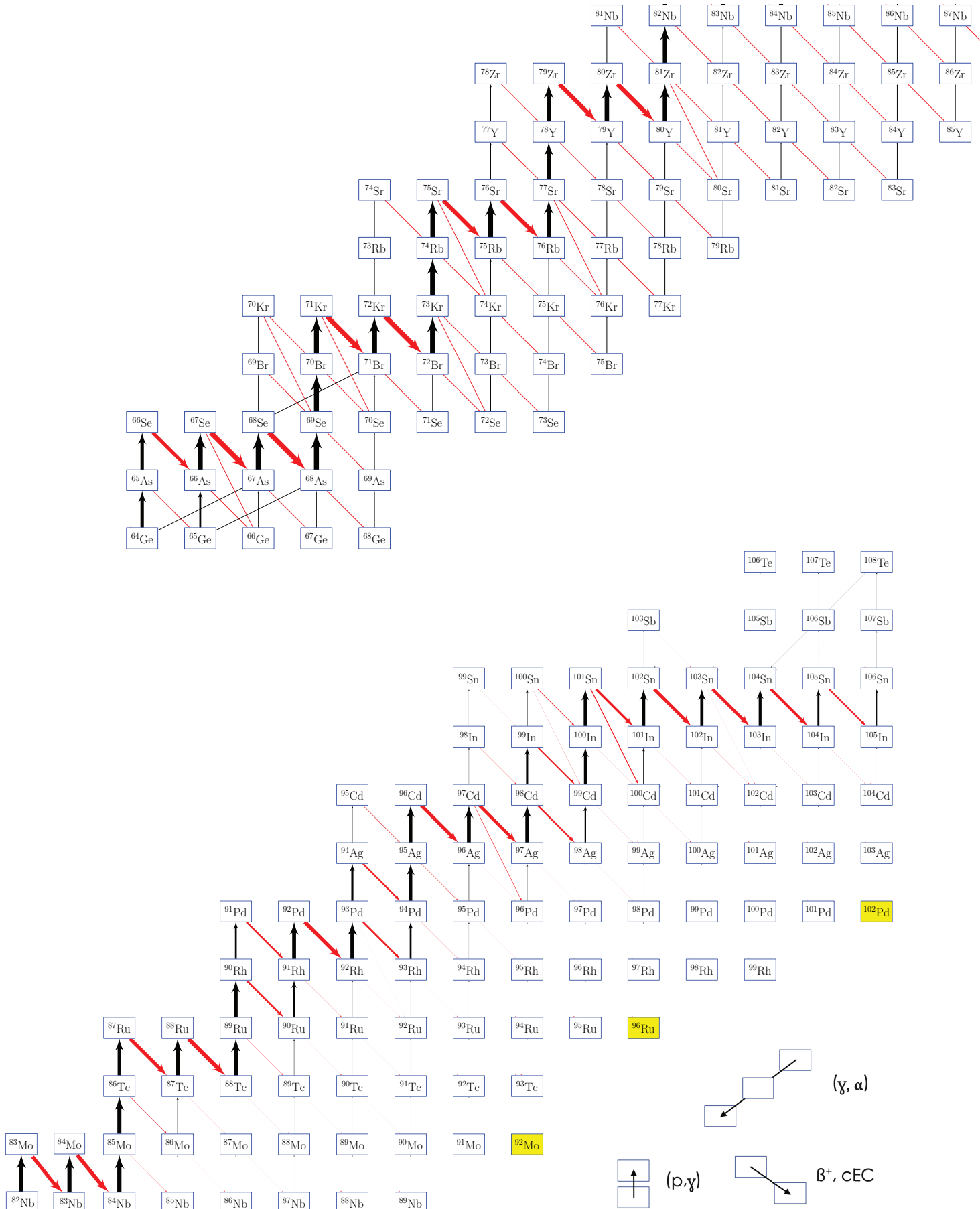


FIG. 6. Integrated reaction currents above Ge during an x-ray burst ( $\approx 210$  sec from the ignition) for the hhez1 composition [2] using the EXVAM results for the temperature dependence of  $\beta^+$ -decay and temperature and density variation of cEC rates for  $^{68}\text{Se}$  and  $^{72}\text{Kr}$  (see text for details). In the online version stable nuclei are yellow while in the print version are grey.

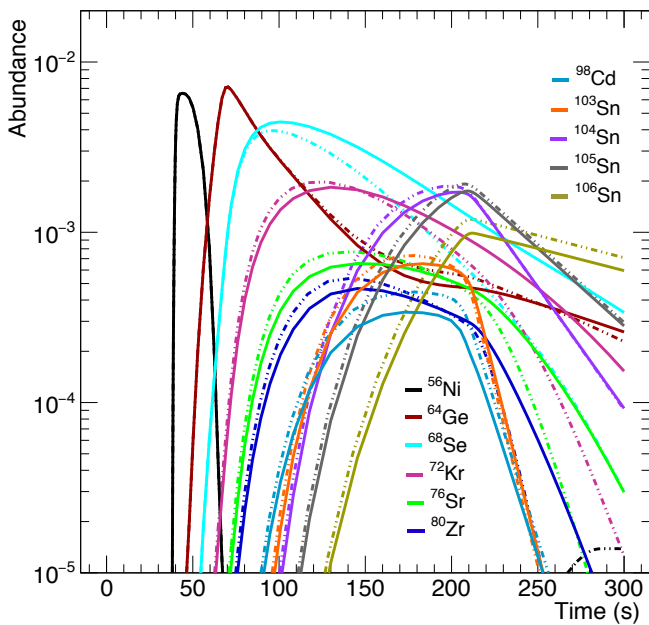


FIG. 7. The evolution of waiting point nuclei and  $^{103-106}\text{Sn}$  isotope abundances using the EXVAM weak rates (dotted-dashed lines) are compared to the results obtained using standard values (full lines) (hhez1 composition [2]).

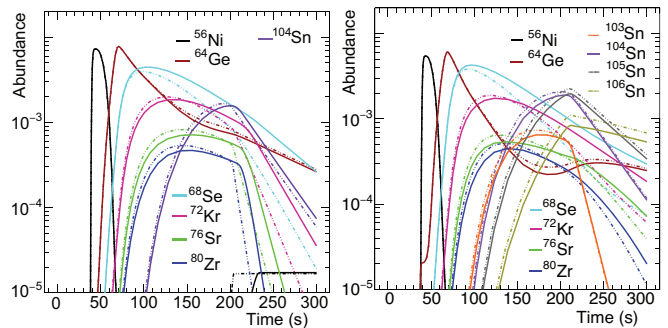


FIG. 8. The abundances of waiting point nuclei and Sn isotopes as a function of time during an x-ray burst obtained using the  $^{68}\text{Se}$  and  $^{72}\text{Kr}$  EXVAM weak interaction rates (dotted-dashed line) compared to that based on standard rates (full line) (left - hhez2; right - hhez3 composition).

burst. Of course, a self-consistent analysis with a hydrodynamic code suitably adjusting both the temperature and the density of the stellar envelope (suggested by the revealed change in energy generation) coupled to nuclear networks including our predictions for the weak interaction rates is necessary to reliably evaluate the considered effects, and we look forward to those calculations. In the mean time, our results on the impact of realistic stellar weak interaction rates for the  $^{68}\text{Se}$  and  $^{72}\text{Kr}$  waiting point nuclei point towards improved estimates of x-ray burst nucleosynthesis, and consequently, of the final abundances of the x-ray bursts required for modelling neutron star crust properties.

#### ACKNOWLEDGMENTS

The authors thank H. Schatz for providing the burst profiles. Part of this work has been supported by the Romanian Ministry for Research and Innovation, project CERN-RO-ISOLDE 03/2016 and Program Nucleu PN-19060103. B. S. M. gratefully acknowledges funding from NASA grant NNX17AE32.

- 
- [1] H. Schatz *et al.*, Phys. Rep. **294**, 167 (1998).
  - [2] H. Schatz *et al.*, Phys. Rev. Lett. **86**, 3471 (2001).
  - [3] S. E. Woosley *et al.*, Astrophys. J. Suppl. Ser. **151**, 75 (2004).
  - [4] A. Parikh, J. Jose, F. Moreno, and C. Iliadis, Astrophys. J. Suppl. Ser. **178**, 110 (2008).
  - [5] H. Schatz and W. J. Ong, Astrophys. J. **844**, 139 (2017).
  - [6] G. M. Fuller, W. A. Fowler, M. J. Newman, Astrophys. J. Suppl. Ser. **42**, 447 (1980); Astrophys. J. **252**, 715 (1982); Astrophys. J. Suppl. Ser. **48**, 279 (1982); Astrophys. J. **293**, 1 (1985).
  - [7] J. Pruet and G. M. Fuller, Astrophys. J. Suppl. Ser. **149**, 189 (2003).
  - [8] K. Langanke and G. Martinez-Pinedo, Nucl. Phys. A **673**, 481 (2000).
  - [9] P. Möller, J. R. Nix, K. -L. Kratz, At. Data Nucl. Data Tables **66**, 131 (1997).
  - [10] P. Sarriguren, Phys. Lett. B **680**, 438 (2009); Phys. Rev. C **83**, 025801 (2011).
  - [11] J.-U. Nabi, Astrophys. Space Sci. **339**, 305 (2012).
  - [12] J.-U. Nabi and M. Bökükata, Nucl. Phys. A **947**, 182 (2016).
  - [13] A. Petrovici, K. W. Schmid, O. Radu, A. Faessler, Phys. Rev. C **78**, 044315 (2008).
  - [14] A. Petrovici, K. W. Schmid, O. Andrei, A. Faessler, Phys. Rev. C **80**, 044319 (2009).
  - [15] A. Petrovici, K. W. Schmid, A. Faessler, Prog. Part. Nucl. Phys. **66**, 287 (2011).
  - [16] A. Petrovici, Phys. Rev. C **91**, 014302 (2015).
  - [17] A. Petrovici and O. Andrei, Eur. Phys. J. A **51**, 133 (2015).

- [18] A. Petrovici and O. Andrei, Phys. Rev. C **92**, 064305 (2015).
- [19] A. Petrovici, Phys. Rev. C **97**, 024313 (2018).
- [20] A. Petrovici, O. Andrei, A. Chilug, Phys. Scr. **93**, 114001 (2018).
- [21] R. H. Cyburt *et al.*, Astrophys. J. **830**, 55 (2016).
- [22] A. Parikh, J. Jose, C. Iliadis, F. Moreno, T. Rauscher, Phys. Rev. C **79**, 045802 (2009).
- [23] R. H. Cyburt *et al.*, Astrophys. J. Suppl. Ser. **189**, 240 (2010).
- [24] <https://sourceforge.net/p/nucnet-tools/home/Home>.
- [25] A. Obertelli *et al.*, Phys. Rev. C **80**, 031304(R) (2009).
- [26] H. Iwasaki *et al.*, Phys. Rev. Lett. **112**, 142502 (2014).
- [27] J. Savory *et al.*, Phys. Rev. Lett. **102**, 132501 (2009).
- [28] J. A. Clark *et al.*, Phys. Rev. Lett. **92**, 192501 (2004).
- [29] D. Rodriguez *et al.*, Eur. Phys. J. A **25**, 41 (2005).
- [30] A. A. Valverde *et al.*, Phys. Rev. C **91**, 037301 (2015).
- [31] E. A. Mccutchan, Nucl. Data Sheets **113**, 1735 (2012).
- [32] D. Abriola and A. A. Sonzogni, Nucl. Data Sheets **111**, 1 (2010).
- [33] M. Ichimura, H. Sakai, T. Wakasa, Progr. Part. Nucl. Phys. **56**, 446 (2006).
- [34] P. Baumann *et al.*, Phys. Rev. C **50**, 1180 (1994).
- [35] I. Piqueras *et al.*, Eur. Phys. J. A **16**, 313 (2003).
- [36] J. A. Briz *et al.*, Phys. Rev. C **92**, 054326 (2015).